

# Dalton Transactions

An international journal of inorganic chemistry

Accepted Manuscript

This article can be cited before page numbers have been issued, to do this please use: M. Chen, D. S. Butenko, I. V. Odynets, I. Zatovsky, J. Li, W. Han and N. Klyui, *Dalton Trans.*, 2020, DOI: 10.1039/D0DT01205J.



This is an Accepted Manuscript, which has been through the Royal Society of Chemistry peer review process and has been accepted for publication.

Accepted Manuscripts are published online shortly after acceptance, before technical editing, formatting and proof reading. Using this free service, authors can make their results available to the community, in citable form, before we publish the edited article. We will replace this Accepted Manuscript with the edited and formatted Advance Article as soon as it is available.

You can find more information about Accepted Manuscripts in the [Information for Authors](#).

Please note that technical editing may introduce minor changes to the text and/or graphics, which may alter content. The journal's standard [Terms & Conditions](#) and the [Ethical guidelines](#) still apply. In no event shall the Royal Society of Chemistry be held responsible for any errors or omissions in this Accepted Manuscript or any consequences arising from the use of any information it contains.

## ARTICLE

# Nanoparticles $\text{Na}_4\text{Ni}_3\text{P}_4\text{O}_{15}$ - $\text{Ni}(\text{OH})_2$ Core-Shell as hybrid electrocatalyst for the oxygen evolution reaction in alkaline electrolyte

Received 00th January 20xx,  
Accepted 00th January 20xx

DOI: 10.1039/x0xx00000x

Chen Mu,<sup>a</sup> Denys S. Butenko,<sup>b</sup> Ievgen V. Odynets,<sup>a,c</sup> Igor V. Zatovsky,<sup>\*a</sup> Junzhi Li,<sup>b</sup> Wei Han,<sup>b,d</sup> and Nikolai I. Klyui<sup>\*a,e</sup>

There are wide interests in developing efficient, robust and low-cost electrode materials for electrolysis of water to produce clean hydrogen fuel. It is especially important to improve the performance and durability of electrocatalysts for OER. Here we showed that the transformation of nanoparticles (n-NNP) and crystalline (c-NNP) forms of mixed phosphate  $\text{Na}_4\text{Ni}_3(\text{PO}_4)_2\text{P}_2\text{O}_7$  in highly alkaline solutions occurs along various routes and provokes generation of 2D-nanosheets  $\text{Ni}(\text{OH})_2$  or stable particles of core(phosphate)-shell( $\text{Ni}(\text{OH})_2$ ), respectively. In both cases, in carbon matrix (through chemical and electrochemical conversion of phosphate *in situ* during electrolysis in 6 M KOH or NaOH solution) stable OER electrocatalysts with low overpotentials of 250–290 mV at a current density of 10 mA·cm<sup>-2</sup> were obtained. The best candidate for OER process is core-shell particles, which maintain overpotentials of around 250 mV in 6 M KOH more than 3 days. The activity enhancement can be attributed to formation of abundant system of NiOOH nanoparticles on the shell surface due to improved lattice matching. The report discusses further prospects for the creation of core-shell particles to reduce the overpotential of durable electrocatalysts for OER.

## Introduction

It is widely known that hydrogen is an environmentally friendly and highly efficient “ideal” fuel. Among the various advanced technologies, hydrogen production by electrolysis is one of the most attractive trends.<sup>1</sup> At the same time, during the process of water oxidation significant overpotentials are required for the oxygen and hydrogen evolution reaction, OER and HER respectively, which leads to additional energy losses. Thus, intensive research is carried out to develop a variety of electrocatalysts that can shift the water splitting potentials closer to the thermodynamic limits.<sup>1–3</sup> First of all, there is demand to fabricate an effective electrocatalysts for OER, since this reaction is the “bottleneck” of water splitting and involves four successive processes.<sup>2,3</sup> Currently,  $\text{RuO}_2$  or  $\text{IrO}_2$  with low

overpotential values are taken as reference electrocatalysts for OER.<sup>4</sup> However, the high cost and low abundance of these noble metals in the soil are unfavorable factor for their widespread application. Therefore, over the past decades, a large number of borides,<sup>5</sup> nitrides,<sup>6,7</sup> oxides or hydroxides,<sup>8–16</sup> phosphides<sup>17–21</sup> and chalcogenides<sup>18,22</sup> of transition metals have been proposed as effective and economically competitive electrocatalysts for OER process.<sup>3</sup> In particular, good catalytic activity was found for various complex oxides with different types of crystal lattice (spinel's, perovskites, etc.).<sup>23–30</sup> It has been shown that amorphous phosphate films<sup>31–34</sup> and crystalline phosphates of *d*-metals<sup>31–42</sup> demonstrate a very high catalytic efficiency in the reaction of gaseous oxygen production.

In recent years, interest in phosphate electrocatalysts for water splitting has increased significantly.<sup>43</sup> Remarkable catalytic features have been found in *d*-metal phosphates with different composition and structure, such as  $\text{FePO}_4$ ,<sup>44</sup>  $\text{Co}_3(\text{PO}_4)_2$ ,<sup>45</sup>  $\text{Co}_3(\text{PO}_4)_2 \cdot 8\text{H}_2\text{O}$ ,<sup>46</sup>  $(\text{Co}_{0.5}\text{Ni}_{0.5})_3(\text{PO}_4)_2$ ,<sup>41</sup>  $\text{Ni}_2\text{P}_2\text{O}_7 \cdot 8\text{H}_2\text{O}$ ,<sup>47</sup>  $\text{Co}_2 \cdot x\text{Ni}_x\text{P}_2\text{O}_7$ ,<sup>48</sup>  $\text{LiNi}_{0.75}\text{Fe}_{0.25}\text{PO}_4$ ,<sup>49</sup>  $\text{Li}(\text{Ni},\text{Fe})\text{PO}_4$ ,<sup>35</sup>  $\text{AFePO}_4$  (A – Na, K),<sup>50</sup>  $\text{NaCoPO}_4$ ,<sup>51</sup>  $\text{Na}_2\text{CoP}_2\text{O}_7$ <sup>38</sup> and etc. Meanwhile in recent years, several new phosphates, for instance  $\text{Ni}_2\text{P}_4\text{O}_{12}$ ,<sup>52</sup>  $(\text{NiFe})\text{PO}_4(\text{OH})$ <sup>53</sup> and  $\text{NaCo}(\text{PO}_3)_3$ <sup>54</sup> were included into the group of effective electrocatalysts.

It should be noted that it is possible to draw a clear parallel dependency between a lot of high voltage cathodes for Li or Na batteries<sup>55,56</sup> and electrocatalysts for OER process based on phosphate materials. A significant number of phosphate structures (frames) is capable to stabilize *d*-metals in various oxidative states, which is a perfect precondition for the presence of catalytic properties for oxidative-reduction

<sup>a</sup> College of Physics, Jilin University, Changchun 130012, P. R. China. E-mail: [zvigo@yandex.ru](mailto:zvigo@yandex.ru), [klyuini@ukr.net](mailto:klyuini@ukr.net)

<sup>b</sup> Sino-Russian International Joint Laboratory for Clean Energy and Energy Conversion Technology, College of Physics, Jilin University, Changchun 130012, P. R. China.

<sup>c</sup> Department of Chemistry, Pavla Tychyina Uman State Pedagogical University, 2 str. Sadova, Uman 20300, Ukraine.

<sup>d</sup> International Center of Future Science, Jilin University, Changchun City 130012, P. R. China.

<sup>e</sup> V. Lashkaryov Institute of Semiconductor Physics, NAS of Ukraine, 41 pr. Nauki, 03028 Kyiv, Ukraine.

†Electronic Supplementary Information (ESI) available: Additional photomicrographs, SEM image and elemental mapping, XRD powder data, TEM images and TEM of high-resolution, XPS spectra, additional electrochemical measurements, section “Electrochemical measurements”, section “Crystallization of the  $\text{Na}_4\text{Ni}_3\text{P}_4\text{O}_{15}$  melt”, section “Investigation of crystallization process from Na-Ni-P-O self-fluxes”, and Table S1-S3. See DOI: 10.1039/x0xx00000x

transformations. Thus, in<sup>35</sup> the process of electrochemical tuning of olivine-type  $\text{Li}(\text{Ni},\text{Fe})\text{PO}_4$  phosphates (widely-researched family of cathode materials in lithium ion batteries) is described. In the study of this material in order to effectively increase the efficiency of using  $\text{LiMPO}_4$  for OER in aqueous solution (generating a current density of  $10 \text{ mA}\cdot\text{cm}^{-2}$  at an overpotential of only  $0.27 \text{ V}$  in  $0.1 \text{ M KOH}$ ), the strategy of partial extraction of lithium ions from phosphate in the organic electrolyte was successfully implemented. Another example is  $\text{NaCo}(\text{PO}_3)_3$ . In 2018, it was shown the possibility of using this compound as a cathode material for sodium ion batteries.<sup>57</sup> And in the next year it was found that this phosphate shows electrocatalytic properties for OER with very small overpotential of  $340 \text{ mV}$  and high mass activity of  $532 \text{ A}\cdot\text{g}^{-1}$ .<sup>54</sup> Thus, in general, we can assume that phosphate cathode materials are potential candidates for OER catalysts. However, there is a significant difference between non-water high voltage ion batteries and water solutions for electrolysis. Under the action of aggressive water electrolytes, especially in the case of alkaline media, *d*-metal phosphates can partially or completely transform into other forms, which leads to changes of catalytic activity. Unfortunately, only a small number of works devoted to phosphate electrocatalysts analyzes this issue. Thus, for Co-contained compounds  $\text{Co}_2(\text{PO}_4)_3$ <sup>42</sup> and  $\text{Na}_4\text{Co}_3\text{P}_4\text{O}_{15}$ <sup>58</sup> *in situ* transformation into forms of cobalt oxide/hydroxide was found, resulting in a general decrease in catalytic activity. Instead, for nickel-phosphate films, the formation of nickel oxyhydroxide ( $\text{NiOOH}$ ) in  $1 \text{ M KOH}$  during water oxidation proceeded only on the surface of phosphate.<sup>31</sup> Obtained hybrid composite shows unique catalytic properties: overpotential  $220$  and  $290 \text{ mV}$  at a current density of  $10$  and  $500 \text{ mA}\cdot\text{cm}^{-2}$  ( $1 \text{ M KOH}$ ), respectively, as well as  $332 \text{ mV}$  at a high current density of  $1600 \text{ mA}\cdot\text{cm}^{-2}$  ( $5 \text{ M KOH}$ ). The authors argue that  $\text{Ni}(\text{Fe})\text{OOH}$  serves as the main catalyst for OER, and phosphate as a co-catalyst for water adsorption.<sup>31</sup> Also, remarkable electrocatalytic performances were observed in case of joint use of phosphates and phosphides (core-shell structure  $\text{Ni}_{12}\text{P}_5\text{-Ni}_3(\text{PO}_4)_2$ ) in alkaline media<sup>59</sup> or in the occurrence of phosphate co-catalysts *in situ* for  $\text{NiCoP}$  nanosystems.<sup>19</sup> In all cases, the presence of a composite material (phosphate-oxide/hydroxide or phosphide-phosphate-oxide/hydroxide) contributes to decrease in the oxygen overpotential values and high catalytic stability over time.<sup>19,31,59,60</sup> Thus, the application of phosphorus-containing materials for production of hybrid catalysts *in situ* is a very attractive idea.<sup>60-65</sup> Structural type diversity of *d*-metal phosphates determines their different stability in alkaline medium. At the same time, a systematic study of this class of compounds have not been carried out yet.

Complex phosphate  $\text{Na}_4\text{Ni}_3\text{P}_4\text{O}_{15}$  is promising material for Na-ion batteries<sup>66</sup> and supercapacitor.<sup>67</sup> In this work we investigated mixed phosphate  $\text{Na}_4\text{Ni}_3(\text{PO}_4)_2\text{P}_2\text{O}_7$  as potential candidate for electrocatalytic water splitting. Here we describe synthesis features of nanoparticles and crystals for this phosphate, which are converted in various ways in an alkaline medium. Both final forms ( $\text{Ni}(\text{OH})_2$  nanosheets and  $\text{Na}_4\text{Ni}_3\text{P}_4\text{O}_{15}\text{-Ni}(\text{OH})_2$  particles with a core-shell structure) can be used as excellent electrocatalysts for OER. As a catalyst for

OER,  $\text{Na}_4\text{Ni}_3\text{P}_4\text{O}_{15}\text{-Ni}(\text{OH})_2/\text{CC}$  electrode showed highly efficient electrocatalytic characteristics with an overpotential of  $250 \text{ mV}$  at  $10 \text{ mA}\cdot\text{cm}^{-2}$  and excellent stability (at least  $70$  hours with continuous electrolysis). Further prospects and ways of creating effective catalysts for core-shell nanoparticles were also analyzed and discussed.

## Experimental

### Synthesis of nanoparticles and crystal form of $\text{Na}_4\text{Ni}_3\text{P}_4\text{O}_{15}$

All used reagents ( $\text{NaH}_2\text{PO}_4\cdot 2\text{H}_2\text{O}$ ,  $\text{Na}_2\text{HPO}_4\cdot 12\text{H}_2\text{O}$ ,  $\text{NH}_4\text{H}_2\text{PO}_4$ ,  $\text{NiO}$ ,  $\text{Ni}(\text{NO}_3)_2\cdot 6\text{H}_2\text{O}$  and  $\text{NH}_3\cdot \text{H}_2\text{O}$  25 % aqueous solution) have analytical grade. The anhydrous powders of  $\text{NaPO}_3$  and  $\text{Na}_4\text{P}_2\text{O}_7$  were prepared by dehydration of  $\text{NaH}_2\text{PO}_4\cdot 2\text{H}_2\text{O}$  and  $\text{Na}_2\text{HPO}_4\cdot 12\text{H}_2\text{O}$  at  $450^\circ\text{C}$  and  $900^\circ\text{C}$  (in a platinum cup), respectively.

Synthesis nanoparticles of  $\text{Na}_4\text{Ni}_3\text{P}_4\text{O}_{15}$ :  $3.989 \text{ g Na}_4\text{P}_2\text{O}_7$ ,  $3.452 \text{ g NH}_4\text{H}_2\text{PO}_4$  and  $13.082 \text{ g Ni}(\text{NO}_3)_2\cdot 6\text{H}_2\text{O}$  were dissolved in  $50 \text{ ml}$  distilled water with stirring to make homogenous solution. Aqueous ammonia was added to the prepared solution to value the pH about  $7.0$ . The solution was then evaporated at  $180^\circ\text{C}$  and the resulting powder was calcined at  $600^\circ\text{C}$  for  $2 \text{ h}$  in air atmosphere. As-prepared of  $\text{Na}_4\text{Ni}_3\text{P}_4\text{O}_{15}$  (n-NNP) is a rounded conglomerates of nanoparticles with diameter to  $0.5 \text{ }\mu\text{m}$  in size of light yellow color (see ESI †, Fig. S1a).

For preparation of crystal form  $\text{Na}_4\text{Ni}_3\text{P}_4\text{O}_{15}$  (c-NNP):  $10.64 \text{ g Na}_4\text{P}_2\text{O}_7$ ,  $12.24 \text{ g NaPO}_3$  and  $4.04 \text{ g NiO}$  were mixed and grounded in an agate mortar. The mixture was melted in platinum crucible at  $1000^\circ\text{C}$  and kept in isothermal conditions for  $5$  hours. Then homogeneous flux was cooled at a rate  $20^\circ\text{C}\cdot\text{h}^{-1}$  down to  $700^\circ\text{C}$ . The crystals were washed from the rest of the melt components with hot distilled water, followed by drying at  $120^\circ\text{C}$  in an air atmosphere oven for  $1 \text{ h}$ . The resulting needle-like crystals (up to  $1 \text{ cm}$  long) have a yellow-orange color and form splices (see ESI †, Fig. S1b).

### Material characterization

Powdered X-Ray diffraction (XRD) patterns were recorded at room temperature using a Shimadzu XRD-6000 X-ray powder diffractometer (Cu radiation with  $\lambda \text{ Cu}_{K\alpha 1} = 1.54056 \text{ \AA}$ ,  $\lambda \text{ Cu}_{K\alpha 2} = 1.54439 \text{ \AA}$  and graphite counter monochromator). Data has been collected from  $5$  to  $70^\circ$  in step scan mode  $2\theta$  (step  $0.02^\circ$  and account time of  $2 \text{ s}$  per point). Transmission XRD pattern was measured on Rigaku MicroMax-007HF (with  $\text{Cu}_{K\alpha}$  radiation). The reference patterns of the crystalline compounds from the PDF2 database were used to identify the samples. The microstructure, morphology and element compositions of the samples were analyzed using scanning electron microscopy (SEM, Magellan 400, recorded at  $10 \text{ kV}$ ) and transmission electron microscopy (TEM, JEOL JSM 2010F, recorded at  $200 \text{ kV}$ ). The FTIR-spectra were obtained in range  $400\text{--}4000 \text{ cm}^{-1}$  at a room temperature using Shimadzu IRAffinity-1S spectrometer (samples were pressed into discs with KBr). The surface chemical states of the catalysts were analyzed using X-ray photoelectron spectroscopy (XPS) measurements performed on a VG ESCALAB MK II electron spectrometer.

### Fabrication of electrodes

For the fabrication of electrodes, the crystals of c-NNP were ground. Crystalline form of  $\text{Na}_4\text{Ni}_3\text{P}_4\text{O}_{15}$  were manually milled in an agate mortar, then in a planetary mill (alcohol media; grinding time 1 h; milling speed of 565 rpm;  $\text{ZrO}_2$  balls with diameter of 10 mm; balls to powder ratio = 10:1 wt.). As a result, powder with a size less than 10  $\mu\text{m}$  was obtained (Fig. S2, ESI †). To manufacture of working electrode the powder of n-NNP or c-NNP was mixed together with conductive carbon black ("Super P") and polyvinylidene fluoride (PVDF) in a weight ratio of 85:10:5, respectively. Then the cream-like slurry was prepared by adding N-methylpyrrolidone (NMP), pasted onto a carbon fiber (HCP331N, 1×1  $\text{cm}^2$  working area) and finally dried at 100°C for 24 h in a vacuum oven. SEM image and elemental mapping of electrodes show mosaic distribution of  $\text{Na}_4\text{Ni}_3\text{P}_4\text{O}_{15}$  particle agglomerations, monotonically surrounded by carbon material (Fig. S3, ESI †).  $\text{IrO}_2$  (Aladdin Industrial Corp, Shanghai, China) electrode prepared by the similar way was used as a benchmark. The fabricated electrodes were hereinafter referred to as n-NNP-C/CC, c-NNP-C/CC and  $\text{IrO}_2$ -C/CC.

### Chemical stability test

The test was performed in 6M solutions of sodium or potassium hydroxide. Powder n-NNP or c-NNP ( $\approx 0.2$  g) was immersed into alkali media and left from 1 to 30 days with periodical stirring. Afterward precipitate was filtered, washed by distilled water, dried in air and analyzed (according to XRD, and FTIR-spectra data).

### Electrochemical testing

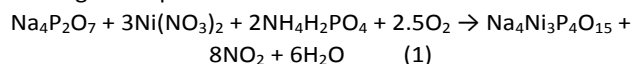
Electrochemical measurements were carried out on an electrochemical analyzer/workstation CH Instruments Model 760E (China). A typical three-electrode set-up was used with a Hg/HgO electrode as a reference electrode and a platinum plate as a counter electrode. Impedance spectroscopy was performed in the frequency range from  $10^5$  to  $10^{-2}$  Hz with the amplitude of 5 mV at the open circuit potential. Multiple cyclic voltammetry (CV) scans were performed for 20 cycles at the scan rate of 10  $\text{mV}\cdot\text{s}^{-1}$  until stable work cell. The linear sweep voltammetry (LSV) curves were collected at the scan rate of 1  $\text{mV}\cdot\text{s}^{-1}$  with iR correction (90%). Chronopotentiometry was carried out under a constant current density of 10  $\text{mA}\cdot\text{cm}^{-2}$  for 20 h or more. Calculations for electrochemical measurements are presented in detail in the section "Electrochemical measurements" ESI †.

## Results and discussion

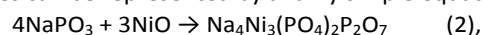
With a purpose to obtain nano (n-NNP) and crystal (c-NNP) form of  $\text{Na}_4\text{Ni}_3\text{P}_4\text{O}_{15}$  we used the results of study given in works.<sup>67,68</sup> But our attempts to synthesize the high-purity form of complex phosphate, as described in these papers, were unsuccessful. Therefore, in both cases, the methods were improved as a result of additional studies.

For the synthesis of n-NNP (according to<sup>67</sup>) the initial reagents  $\text{Na}_4\text{P}_2\text{O}_7$ ,  $\text{Ni}(\text{NO}_3)_2\cdot 6\text{H}_2\text{O}$  and  $\text{NH}_4\text{H}_2\text{PO}_4$  were used. However, the components were taken in proportion to obtain a finite ratio of Na:Ni:P as 4:3:4. Moreover, organic reagents (urea, glycine or

hexamine)<sup>67</sup> as fuel have not been added. Subsequently, the initial mixture of reagents after evaporation of water was calcined at 600°C (similar to<sup>67</sup>). The general scheme of n-NNP obtaining corresponded to the reaction:



In case of c-NNP, synthesis was carried out as described in,<sup>68</sup> but only a mixture of phosphates was obtained (see: Crystallization of the  $\text{Na}_4\text{Ni}_3\text{PO}_{15}$  melt and Fig. S4, ESI †). Therefore, we conducted a comprehensive study of self-flux in Na–Ni–P–O system and found the condition for obtaining single crystals of  $\text{Na}_4\text{Ni}_3\text{P}_4\text{O}_{15}$  without impurities (see: Investigation of crystallization process from Na–Ni–P–O self-fluxes and Table S1, ESI †). Although the crystallization of  $\text{Na}_4\text{Ni}_3(\text{PO}_4)_2\text{P}_2\text{O}_7$  in the self-fluxes can be represented by a fairly simple equation:



but in self-fluxes with an initial Na/P ratio equal to 1.0 this compound is not formed. Only when initial Na/P ratios ranging from 1.3 to 1.5 can be obtained purely of  $\text{Na}_4\text{Ni}_3\text{P}_4\text{O}_{15}$ . A similar situation was observed for many of self-fluxes type  $\text{M}^I\text{–Me–P–O}$  ( $\text{M}^I$  – alkali metals, Me – polyvalent metals).<sup>69–71</sup>

The phase purity of the obtained samples was measured by the XRD characterizations, as shown in Fig. 1a. The positions of the diffraction peaks of n-NNP and c-NNP fully coincide with the PDF card #01-087-0977 which belongs to target product  $\text{Na}_4\text{Ni}_3\text{P}_4\text{O}_{15}$ . Both diffraction patterns show a good preservation of the ratios between the intensities of most part reflexes, example indexed to the [001], [420] + [510], [040] + [620], [222] + [402] crystal planes (Fig. 1a). However, reflexes with double indices [110] + [200], [020] + [310] and [002] + [312] of c-NNP are significantly more intense (Fig. 1a). This fact indicates that the texture of needle-like crystals  $\text{Na}_4\text{Ni}_3\text{P}_4\text{O}_{15}$  (perpendicular to the c-axis of the orthorhombic cell) is present even after a very long grinding of c-NNP.

Typical SEM images for n-NNP are represented in Fig. 1b,c. Spherical agglomerates n-NNP is polydisperse and consists of smaller particles (Fig. 1b). At higher magnification, we can see that the sample consists of nanoparticles less than 1  $\mu\text{m}$  with grain-like structure (Fig. 1c). A similar morphology was also described for nano- $\text{Na}_4\text{Ni}_3\text{P}_4\text{O}_{15}$  in.<sup>67</sup> For both samples, the results of EDX and elemental mapping confirm composition and homogeneous distribution of elements (Fig. S5, ESI †). According to the image of SEM, the sample c-NNP milled in the planetary mill is fragments of single crystals with a size less than 10  $\mu\text{m}$  (Fig. S2, ESI †).

In the FTIR spectra of both samples n-NNP and c-NNP, an identical set of absorption peaks is observed as combination of the vibration modes of the  $\text{PO}_4$  and  $\text{P}_2\text{O}_7$  groups (Fig. 1d). The following frequency regions of the vibration modes of the  $\text{PO}_4$

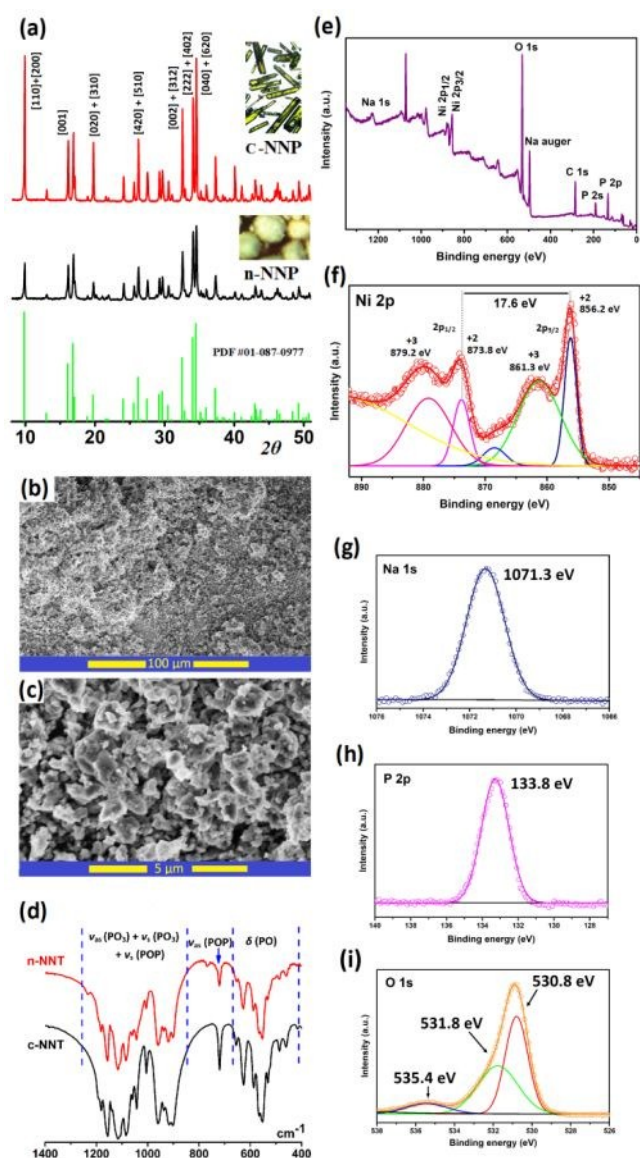


**Fig. 1** (a) The results XRD for c-NNP and n-NNP. (b,c) Typical SEM images at various magnification of n-NNP. (d) FTIR spectra of n-NNP and c-NNP. (e) overall XPS spectrum for c-NNP and high-resolution XPS (f) Ni 2p, (g) Na 1s, (h) P 2p, (i) O 1s.

and  $P_2O_7$  groups can be distinguished in the spectra: the bands in the range of  $650\text{--}400\text{ cm}^{-1}$  belong to  $\delta$  (PO) vibrations; the intense sharp peak at  $720\text{ cm}^{-1}$  corresponds to asymmetric stretching of the P–O–P bonds, which indicates the presence of the  $P_2O_7$  group; the bands in the region of  $850\text{--}1250\text{ cm}^{-1}$  are assigned as  $\nu_{as}$ ,  $\nu_s$  ( $PO_3$ ) and  $\nu_{as}$  (POP) stretching vibrations. This set of absorption peaks is characteristic for an isostructural complex phosphates of general composition  $Na_4M^{II}_3(PO_4)_2P_2O_7$  ( $M^{II} = Fe, Mn, Co, Ni$ ).

According to full XPS survey, the main signals of O 1s, P 2p, Na 1s and Ni 2p elements were detected (Fig. 1e). In the high-resolution Ni 2p spectrum there is a spin-orbit splitting on two energy states Ni  $2p_{3/2}$  (856.2 eV) and Ni  $2p_{1/2}$  (873.8 eV) with an energy gap of 17.6 eV (Fig. 1f). The value of 17.6 eV is close to 17.4 eV, which should be considered as standard for the splitting of  $Ni^{2+}$ .<sup>72</sup> Each of  $Ni^{2+}$  signal is accompanied by satellites

at 879.2 and 861.3 eV (Fig. 1f), which indicates the presence of trivalent nickel.<sup>73</sup> The presence of  $d$ -metals with different oxidation states on the sample surface, in general, is typical situation for  $Na_4M^{II}_3P_4O_{15}$  compounds.<sup>58,67</sup> This factor should be favorable for passing electro-catalytic transformations on the material surface. The position of Na 1s peak located at 1071.3 eV (Fig. 1g) and almost equal to 1073.3 eV which given for  $Na_4Ni_3P_4O_{15}$  in.<sup>67</sup> The singlet peak in the P 1p spectrum at 133.8 eV (Fig. 1h) confirms that phosphorus exists in oxidation state 5+ to form P–O bond.<sup>32,36</sup> Only three peaks with centers at 530.8, 531.8 and 535.4 eV can be distinguished in the O 1s spectrum (Fig. 1i). Peaks with values 530.8 and 531.8 eV should be considered as derivatives of different types of P–O bonds.<sup>32,36</sup> The presence of weak peak at 535.4 eV possibly related to a small amount of physically adsorbed water or other oxygen molecules groups at the surface.<sup>74</sup>

As noted in the introduction,<sup>42,58</sup> complex phosphates under the action of an alkaline media can decompose, which is accompanied by leaching of phosphate anions. Thus, a preliminary test of chemical behavior of phosphate in an alkaline solution allows partial modeling of the conversion processes, which may shed light on the dependencies between the composition and structure of phosphate electrocatalysts in OER conditions. Post-treatment analysis (samples was hold in 6M KOH or NaOH solution) indicates that the decomposition process of n-NNP and c-NNP samples is different. After immersion in an alkaline solution, both samples have changed their initial color from yellow to light green, which is caused by chemical conversion.

In cases of n-NNP, there is a rapid and complete decomposition (less than 1h) of the original sample and formation of  $Ni(OH)_2$ . This interaction can be represented by the next equation:



The formation of pure nickel (II) hydroxide is confirmed by results of XRD and FTIR analysis. On XRD profile can be clearly seen only a few wide and strong diffraction reflections from  $Ni(OH)_2$  (Fig. 6a, ESI †). In addition, broadening of the reflection indicates weak crystalline state of compound. This result is consistent by TEM images (Fig. S6b,c, ESI †):  $Ni(OH)_2$  looks like 2D nanosheets, scattered or bounded into conglomerates. The high-resolution TEM image shown in Fig. S6d ESI † confirms that the  $Ni(OH)_2$  have lattice fringes with interplanar distances of 0.47, and 0.23 nm, corresponding to the [001] and [101] lattice planes of  $Ni(OH)_2$  (PDF # 00-014-0117). In addition, EDX analysis and mapping also indicate complete destruction of n-NNP sample with residual amount of sodium and phosphorus less than 0.25% wt. (Fig. S7 ESI †).

For c-NNP samples, the interaction scheme (3) is also implemented, but the final result is different. According to the XRD data, the phosphate phase is partially retained even after 30 days treatment in an alkaline medium. The XRD profile simultaneously includes wide reflections from  $Ni(OH)_2$  and sharp c-NNP peaks (Fig. S8a, ESI †). The formation of the composite  $Ni(OH)_2$  and c-NNP also confirmed by the results of FTIR spectroscopy (Fig. S8b, ESI †): absorption bands of pristine compound in the region of  $1200\text{--}880\text{ cm}^{-1}$  are still present (vibration modes of  $PO_4/P_2O_7$  groups) while a new intense peak at the  $3643\text{ cm}^{-1}$  have been appeared (vibration mode of O–H bond from  $Ni(OH)_2$ ). TEM studies have clarified this question. These images clearly show that the c-NNP particles are coated with a shell of

Ni(OH)<sub>2</sub>, which apparently protect the core from further destruction by an alkaline solution (Fig. S8c,d, ESI †). Thus, we can state the fact of formation of a stable Na<sub>4</sub>Ni<sub>3</sub>P<sub>4</sub>O<sub>15</sub>-Ni(OH)<sub>2</sub> core-shell structure.

We assume that the differences in the destruction between n-NNP and c-NNP in an alkaline medium are due to the microstructure and peculiarity of the crystal structure of Na<sub>4</sub>Ni<sub>3</sub>P<sub>4</sub>O<sub>15</sub>. The crystalline framework of Na<sub>4</sub>M<sup>II</sup><sub>3</sub>P<sub>4</sub>O<sub>15</sub> (M<sup>II</sup> - divalent 3d-metals) is classified as a layered type of structure, in which fragments from infinite parallel 2D sheets of M<sup>II</sup><sub>3</sub>P<sub>2</sub>O<sub>13</sub> are linked by bridges of P<sub>2</sub>O<sub>7</sub> groups (to 3D framework) and separated by layers of sodium atoms.<sup>68,69</sup> Accordingly, this type of crystalline packing suggests the presence of anisotropy of the growth of the Na<sub>4</sub>Ni<sub>3</sub>P<sub>4</sub>O<sub>15</sub> crystal. As noted above, the appearance of a stable texture perpendicular to the *c* axis occurs for c-NNP (Fig. 1a). The presence of texture indicates anisotropic properties of c-NNP microcrystals. Therefore, the rate of destruction of various faces of the Na<sub>4</sub>Ni<sub>3</sub>P<sub>4</sub>O<sub>15</sub> crystal in an alkaline medium will be different. Respectively, the formation of 2D Ni(OH)<sub>2</sub> films on the c-NNP surface is slower and, as a result, the Na<sub>4</sub>Ni<sub>3</sub>P<sub>4</sub>O<sub>15</sub> microcrystal is wrapped with a shell, which prevents the final destruction. In contrast, n-NNP material consists of nanoparticle conglomerates (without texture) and its destruction in an alkaline solution occurs faster and quantitatively.

In addition, we tested n-NNP and c-NNP samples in 1 M and 0.1 M alkaline solutions (test details and results are presented in section "Chemical stability test in solutions of hydroxides" ESI †). As noted above, noticeable destruction of the n-NNP material in an alkaline solution (including 1M and 0.1 M concentrations) occurs. The rate of Ni(OH)<sub>2</sub> nanosheets formation on the surface of the n-NNP form slows down as alkali concentration in solution decreases. Accordingly, tuning of the core-shell ratio can be carried out by selecting the concentration of the alkaline solution and controlling the exposure time. It should also be noted that we did not observe a noticeable difference in the interaction of phosphates with NaOH and KOH in the same concentration.

In general, the result of the conversion of n-NNP and c-NNP in an alkaline medium is the appearance of Ni(OH)<sub>2</sub> 2D nanosheets, that can be a favorable factor for the electrocatalytic OER process.<sup>8,10,75</sup>

To date, a significant portion of industrial electrolyzers for water splitting uses electrolytes with a high alkaline concentration (20-30%).<sup>76</sup> Thus, for study of OER activity as a part of our electrode developing program, we chose a typical three-electrode cell in 6M NaOH and KOH solutions. As shown in the previous tests, complete (n-NNP) or partial (c-NNP) conversion to the Ni(OH)<sub>2</sub>-form should be expected in an alkaline medium. Accordingly, for fabricated electrodes, there must be a stage of *in situ* transformation of initial material to a stabilized state form. The CV method was used to identify the features of this process. Based on previous CV tests, recorded at different scan speed and in variable intervals within potentials, we found stabilization conditions for electrodes. Overall, for OER activity evaluation and comparison of results was proposed testing algorithm which includes a series of successive measurements of cyclic voltammetry (CV), impedance spectroscopy (AC), linear sweep voltammetry (LSV) and chronopotentiometry (CP).

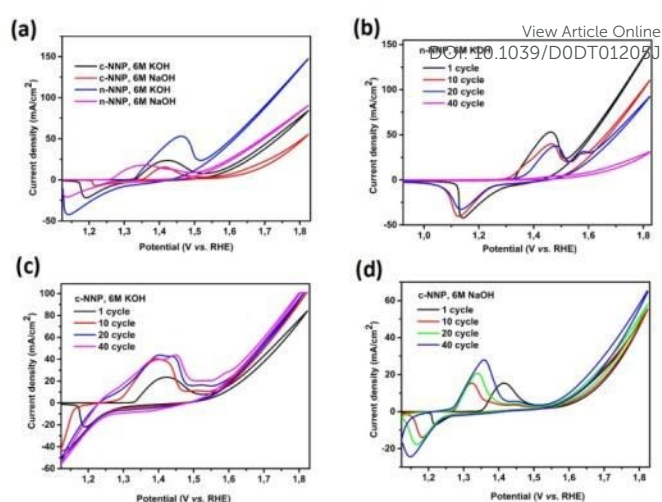


**Fig. 2** Multiple CV of n-NNP-C/CC and c-NNP-C/CC c-NNP electrodes: (a) 1<sup>st</sup> cycle in 6 M KOH and NaOH solutions; (b) 1<sup>st</sup>, 10<sup>th</sup>, 20<sup>th</sup> and 40<sup>th</sup> cycles for n-NNP-C/CC in 6 M KOH; (c) 1<sup>st</sup>, 10<sup>th</sup>, 20<sup>th</sup> and 40<sup>th</sup> cycles for c-NNP-C/CC in 6 M KOH; (d) 1<sup>st</sup>, 10<sup>th</sup>, 20<sup>th</sup> and 40<sup>th</sup> cycles for c-NNP-C/CC in 6 M NaOH. In all case scan rate 10 mV·s<sup>-1</sup>.

Initial CV tests show that behavior of electrodes based on n-NNP and c-NNP is significantly diverse. For all samples within the potential window from 1.1 to 1.85 V (V vs. RHE), two sections can be distinguished on CV curves of the first cycle (Fig. 2a). The first of them in the range 1.2 to 1.5 V corresponds to the nickel-reversible redox transitions Ni<sup>2+</sup> ↔ Ni<sup>3+</sup> ↔ Ni<sup>4+</sup>.<sup>35,36,38</sup> The second section is located above 1.5 V, where the OER passes (gas bubbles are observed on the surface of the electrodes). As can be seen from Fig. 2b, for an electrode n-NNP-C/CC in 6M KOH already in the first cycle at a voltage of 1.85 V, a current density of more than 140 mV·cm<sup>-2</sup> is achieved, and as a consequence there is an extremely intense release of oxygen bubbles, which gradually destroys the surface of the electrode. Upon further cyclization, small particles of the catalytic mass are broken off from the surface of the electrode, which is accompanied by a rapid decrease in catalytic activity.

Already after the 40<sup>th</sup> CV cycle, practically the entire electrode mass is separated from the surface of the CC collector, and the maximum current density does not exceed 35 mV·cm<sup>-2</sup> (Fig. 2b). A similar situation is observed in the case of the 6M NaOH electrolyte (Fig. S9a, ESI †). Accordingly, to stabilize the electrodes n-NNP-C/CC for further studies, CV cycling was performed in the range from 0.85 to 1.45 V (Fig. S9b,c, ESI †), which ensured their integrity. The inverse situation is observed in the case of c-NNP-C/CC (Fig. 2c,d). Already in the first CV cycle, current densities of 55 and 80 mV·cm<sup>-2</sup> for electrolytes based on 6 M NaOH and KOH were reached at a voltage of about 1.85 V. Moreover, with further cyclization, the maximum current density did not decrease, but rather increased (Fig. 2c,d). However, no visual signs of electrode destruction were observed. Additionally, in section 1.1-1.85 V it is clearly seen that as the number of cycles increases, the centers of the nickel oxidation/reduction peaks gradually shift to the left and right, respectively. Moreover, on the CV curves for KOH electrolyte, there is a splitting of the nickel oxidation peak (Fig. 2c), which indicates the simultaneous presence of different nickel-containing phases.

Such a striking difference in the behavior of n-NNP and c-NNP material can be explained in terms of the kinetics of the decomposition of various forms of phosphate in an alkaline solution. As noted above, the interaction of phosphate nanoparticles with alkali occurs rapidly with complete conversion to  $\text{Ni}(\text{OH})_2$ . It can be predicted that the rapid occurrence of large quantities of highly active catalytic forms of  $\text{Ni}(\text{OH})_2$  and  $\text{NiOOH}$  in the middle of a carbon matrix saturated by alkaline solution results in extremely intense oxygen evolution at a voltage rise that does not have time to diffuse to the electrode surface. As a result, a considerable pressure of gas occurs in the bulk of electrode, which leads to the destruction of its base. Instead, for c-NNP-C/CC generation of  $\text{Ni}(\text{OH})_2$  is slow, allowing the electrode to stabilize over time.

After electrode stabilization, impedance spectroscopy (AC imp) measurements were performed, which are presented in Fig. 3a,b. The impedance spectra correlate well with the equivalent circuit shown in Fig. S10, ESI †. The Nyquist plots for all samples are similar in shape and interpreted in Table S2, ESI †. All values of  $R_s$  (including electrolyte and interface resistance) are in the range of 1 to  $1.8 \Omega \cdot \text{cm}^{-2}$ , indicating good catalytic converter contact with a favorable factor for charge transfer. In addition, small values of  $R_{ct}$  (determined by the diameter of the semicircle) within  $4.0\text{--}6.9 \Omega \cdot \text{cm}^{-2}$  correspond to a faster charge transfer of the electrolyte catalyst. These factors are a prerequisite for good catalytic activity.

A subsequent LSV measurement at a scan rate of  $1 \text{ mV} \cdot \text{s}^{-1}$ , comparison with  $\text{IrO}_2$  catalyst and CC current collector is shown in Fig. 3c,d. In the case of n-NNP-C/CC, the LSV curves present an extremely intense peak centered at about 1.4 V, which should be associated with the conversion of  $\text{Ni}(\text{OH})_2$  to  $\text{NiOOH}$  form. For c-NNP-C/CC, this peak is also presented, but it shifted to the lower-voltage region and located at 1.37 and 1.28 V for KOH and NaOH electrolytes, respectively. This indicates differences in catalytic forms for n-NNP and c-NNP. In LSV areas above 1.5 V, there is a rapid increase in current, which leads to the intensive release of oxygen as a result of the OER. In the vast majority of data presented in the literature regarding to the measurement of the electrocatalytic characteristics in an alkaline medium, the results are given generally for 1 M KOH or NaOH solutions. Therefore, for a better understanding of the correlation of the obtained values of overpotential in comparison with those obtained earlier, we conditionally assumed a pH of 14 for 6 M alkalis solutions. Under this condition, against the RHE scale for the LSV 6 M KOH curves at current densities of 100 and  $200 \text{ mV} \cdot \text{cm}^{-2}$ , the overpotential of oxygen evolution are 290 and 330 mV for n-NNP-C/CC and 340 and 380 mV for c-NNP-C/CC. These values are even better than the corresponding result for  $\text{IrO}_2$ -C/CC (360 mV of overpotential at  $100 \text{ mA} \cdot \text{cm}^{-2}$  and 400 mV at  $200 \text{ mA} \cdot \text{cm}^{-2}$ ). In a 6 M NaOH solution, the overpotential values are higher: 360 mV at  $100 \text{ mA} \cdot \text{cm}^{-2}$  and 410 mV at  $200 \text{ mA} \cdot \text{cm}^{-2}$  (n-NNP-C/CC), 380 mV at  $100 \text{ mA} \cdot \text{cm}^{-2}$  and 440 mV at  $200 \text{ mA} \cdot \text{cm}^{-2}$  ( $\text{IrO}_2$ -C/CC) and 480 mV at  $100 \text{ mA} \cdot \text{cm}^{-2}$  and 560 mV at  $200 \text{ mA} \cdot \text{cm}^{-2}$  (c-NNP-C/CC). The CC base of the electrode is generally characterized by low OER conversion activity (Fig. 3c).

Before the CP test, we additionally conducted electrochemical tests of the CC electrode in 6 M alkalis (Fig. S11, ESI †). The results show that the CC current collector is sufficiently stable at a current density of  $10 \text{ mV} \cdot \text{cm}^{-2}$ , however, at  $20 \text{ mV} \cdot \text{cm}^{-2}$ , the destruction of the CC

substrate, accompanied by the electrolyte coloration in black, begins quite intensively. Accordingly, it is to be expected that the

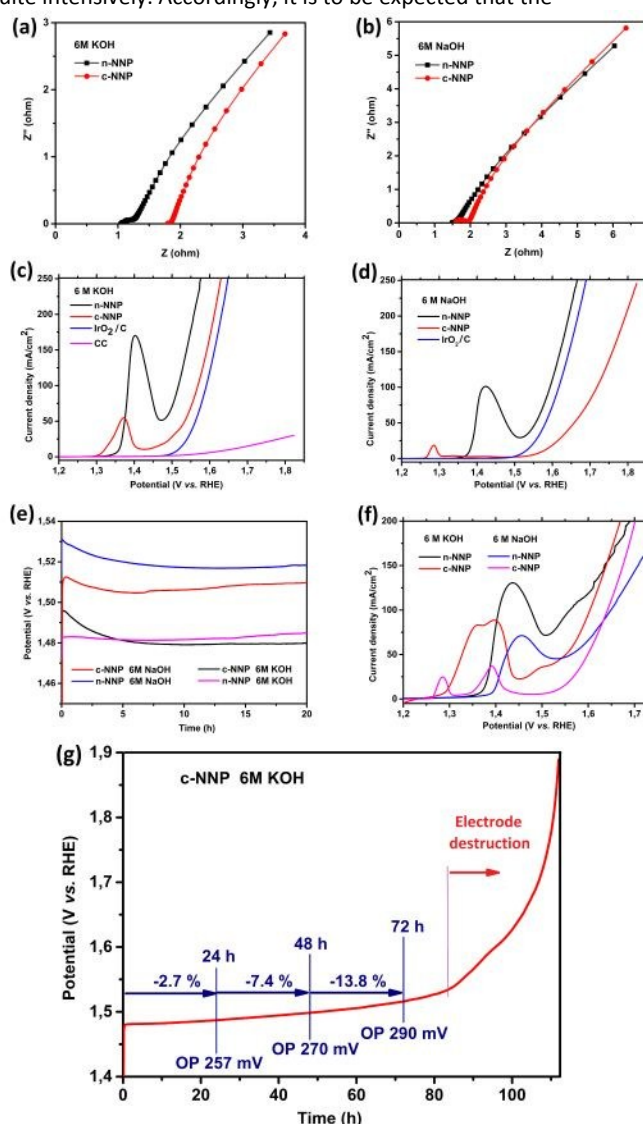


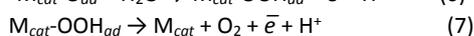
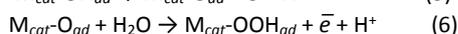
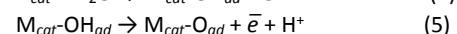
**Fig. 3** Electrochemical measurements for the OER: (a) and (b) AC impedance spectroscopy in 6 M KOH and NaOH, respectively; (c) and (d) polarization curves before the long-term stability test for n-NNP-C/CC, c-NNP-C/CC,  $\text{IrO}_2$ /CC and CC at a scan rate of  $1 \text{ mV} \cdot \text{s}^{-1}$  in 6 M KOH and NaOH, respectively; (e) time dependencies of potential under a constant current density of  $10 \text{ mA} \cdot \text{cm}^{-2}$  for n-NNP-C/CC and c-NNP-C/CC in 6 M KOH and NaOH; (f) LSV curves of c-NNP-C/CC, c-NNP-C/CC at a scan rate of  $1 \text{ mV} \cdot \text{s}^{-1}$  after the long-term stability test in 6 M KOH and NaOH; (g) long-time CP test at a current density of  $10 \text{ mA} \cdot \text{cm}^{-2}$  for n-NNP-C/CC electrode in 6 M KOH (after stabilization of electrode for 10 hours at a current density of  $10 \text{ mA} \cdot \text{cm}^{-2}$ ).

interface of the current collector-electrode material may be impaired, which may interfere with obtaining reliable data during long-term testing. Therefore, at the next stage, CP was performed at a current density of  $10 \text{ mV} \cdot \text{cm}^{-2}$  for 20 h (Fig. 3e). During the first 10 minutes of the test, there is an increase in the voltage, which gradually decreases in the next 5-7 hours and indicates the final stabilization for all electrodes. An interesting fact is that during this time, the initial values for the overpotential of c-NNP-C/CC and n-NNP-C/CC in 6M KOH are reversed, indicating that there is transformation for the c-NNP material (Fig. 3e). After 10 hours of CP test, there is a very

slight increase in voltage (just a few percent). The final values overpotential of oxygen evolution after 20 hours were about 250 mV for c-NNP-C/CC, 260 mV for n-NNP-C/CC (6M KOH), and 280 mV for c-NNP-C/CC, 290 mV for n-NNP-C/CC (6M NaOH).

The results of repeated LSV test after CP process are shown in Fig. 3f. For n-NNP-C/CC electrodes in both electrolytes, a peak about at 1.4 V, whose center is slightly shifted to the higher voltage region (approximately 0.03 V), is presented. Another situation is observed for the c-NNP-C/CC form where the peaks are split. In the case of KOH solution, there are two intense peaks approximately at 1.36 and 1.39 V, and in NaOH solution, the difference increases up to 0.1 V (at 1.28 and 1.38 V). This picture generally confirms the significant difference in electrochemical behavior of n-NNP and c-NNP materials.

It is widely accepted that OER consists of four consecutive stages, according to the next basic Equations:<sup>2,13,38</sup>



In our case, the active catalytic sites are atoms of nickel. These atoms are subject to cyclic transformation of oxidation states: after water adsorption on the active site (4), transitional forms of Ni-O (5) and Ni-OOH (6) subsequently arise, and oxygen is released at the final stage (7). This mechanism is most probable for phosphate<sup>35-38</sup> and oxide/hydroxide catalysts.<sup>8-16</sup>

The fundamental kinetic mechanism of OER, which occurs on the surfaces of the electrocatalysts, is usually described by Tafel plots. Tafel plots are typically determined from the straight-line portion of the LSV in the region of onset of OER conversion. However, in our case, this area significantly overlaps with the broad peaks of electrochemical  $Ni^{2+} \leftrightarrow Ni^{3+}$  transitions (Fig. 3c,d,f), which does not allow a correct calculation. Accordingly, for these calculations, we have performed an additional study of the sample with the best characteristics (c-NNP sample in 6 M KOH solution). A thin layer of this electrode material was deposited on a titanium mesh and after electrode stabilization electrochemical tests were performed (details and descriptions of these studies are given in Fig. S12). The calculated Tafel plot for c-NNP-C/Ti was evaluated as  $74.2 \text{ mV}\cdot\text{dec}^{-1}$ , which shows good catalytic activity against the standard  $IrO_2$ -C/CC electrode with Tafel equal to  $55.7 \text{ mV}\cdot\text{dec}^{-1}$  in 6M KOH (Fig. S12, ESI †).

For a deeper understanding of the features *in situ* transformation features of n-NNP and c-NNP forms in alkaline electrolytes after long-time electrochemical treatment, we examined the electrodes by diverse methods. EDX analysis and elemental mapping show that for n-NNP-C/CC (Fig. S13, ESI †) and c-NNP-C/CC (Fig. 4a) in comparison with initial substance the elemental composition is converted in different ways. In case of n-NNP-C/CC, phosphate is completely destroyed: nickel and oxygen are identified on the electrode surface, but phosphorus, sodium and potassium are present in very low quantities, only as an impurity (Fig. S13, ESI †). Whereas, for c-NNP-C/CC only a slight decreasing of content was observed for phosphorus, lesser for sodium, while for nickel and oxygen remained practically unchanged (Fig. 4a). Moreover, the particles shape and their total distribution on the surface of the electrode have not changed. Comparison of FTIR spectra of c-NNP-C/CC before and after

CP test (Fig. 4b) confirms noticeable degradation of phosphate phases in process of water splitting

DOI: 10.1039/D0DT01205J

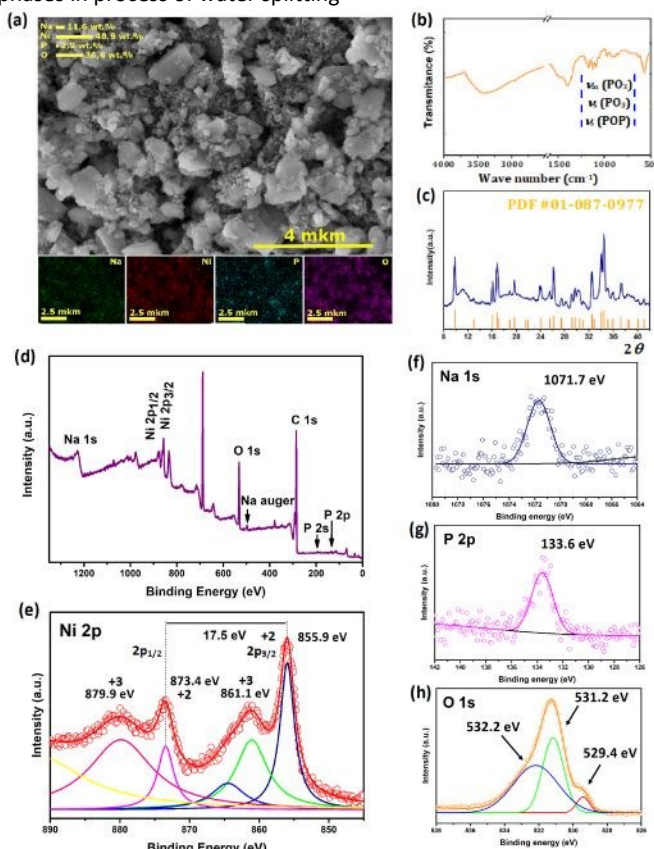


**Fig. 4** The results of the study of c-NNP-C/CC electrode after the long-term stability test for OER in 6 M KOH: (a) SEM image, EDX analysis and elemental mapping; (b) FTIR spectra; (c) transmission XRD profile; (d) overall XPS spectrum and high-resolution XPS (e) Ni 2p, (f) Na 1s, (g) P 2p, (h) O 1s.

(similar changes in the FTIR spectrum were observed for c-NNP material after chemical treatment in alkaline solution, Fig. S8b, ESI †). On transmission XRD profile of c-NNP-C/CC measured after CP test only one type of phase can be clearly distinguished, this phase is initial phosphate (Fig. 4c). This suggests the presence of an amorphous phase on the surface of phosphate. As described above, the interaction of  $Na_4Ni_3P_4O_{15}$  with an alkaline solution leads to the formation of nickel hydroxide. At the same time, it is well known that the nickel hydroxide is transformed to nickel oxyhydroxide (NiOOH) in the conditions of the OER process.<sup>11-15</sup>

This transformation pathway is consistent with results of XPS spectroscopy. As it should be expected in the XPS spectra signals of O 1s and Ni 2p elements of the n-NNP-C/CC electrode after the CP test were detected, whereas the spectrum of P 2p and Na 1s are absent (Fig. S14a,c,d, ESI †). The Ni 2p core-level XPS spectra are displayed in Fig. S14b, in which Ni  $2p_{3/2}$  (856.0 eV) and Ni  $2p_{1/2}$  (873.7 eV) with an energy gap of 17.7 eV were assigned to  $Ni^{2+}$  in  $Ni(OH)_2$  (Fig. S14b, ESI †).<sup>72,75</sup> Two more intense peaks at 861.9 eV and 880.7 eV correspond to  $Ni^{3+}$  in NiOOH.<sup>73</sup> Moreover, the O1s high-resolution spectra (Fig. S14e, ESI †) showed only two peaks at 531.2 eV and 532.1 eV due to the presence Ni–O and –OH groups, respectively.<sup>77,78</sup> Accordingly, the transformation of n-NNP to  $Ni(OH)_2$  occurs in an alkaline solution, but an additional oxidative condition of the OOR process causes a partial conversion of  $Ni(OH)_2 \rightarrow NiOOH$ .

It should be noted that XPS spectra of the c-NNP-C/CC electrode after long-term CP measurement (Fig. 4d-h) can be only partially be considered as a superposition XPS spectra of c-NNP and  $\text{Ni}(\text{OH})_2 + \text{NiOOH}$  (n-NNP-C/CC after CP). In the high-resolution XPS spectra, the positions of the peaks for Na 1s at 1071.7 eV (Fig. 4f) and P 2p at 133.6 eV (Fig. 4g) are very close to the values obtained for pure c-NNP (Fig. 1). This fact clearly indicates a partial conservation of the initial c-NNP phosphate. At the same time, changes are occurring in the high-resolution spectra of Ni 2p and O 1s. Thus, a certain shift is observed both for the more intense peaks at 855.9 eV and 873.4 eV (Ni 2p<sub>3/2</sub> and Ni 2p<sub>1/2</sub> with an energy gap of 17.5 eV) related to Ni<sup>2+</sup>, and less intense at 861.1 eV and 879.9 eV due to the presence of Ni<sup>3+</sup> (Fig. 4e). Moreover, in the O 1s spectrum, in addition to the peaks at 531.2 eV and 532.2 eV (corresponding to Ni–O and –OH for  $\text{Ni}(\text{OH})_2 + \text{NiOOH}$ , Fig. S14e, ESI †), and peak of 529.4 eV are observed (Fig. 4h), which indicates the presence of additional types of Ni–O bonds. New types of Ni–O bonds and peaks shift in the high resolution spectra of Ni 2p indicate to the emergence of an additional binding interface for c-NNP material and  $\text{Ni}(\text{OH})_2 + \text{NiOOH}$  coverings. This can provide a stable core-shell system (nanoparticles  $\text{Na}_4\text{Ni}_3\text{P}_4\text{O}_{15}$ - $\text{Ni}(\text{OH})_2$  core-shell).

Visualization of transformed c-NNP particles after long-term CP was performed using TEM. Fig. 5 shows TEM images at various magnifications. It can be seen that the surface of the n-NNP material is covered with a dense shell composed of small particles (Fig. 5a). At a larger magnification (Fig. 5b,c), it becomes visible that the shell consists of nanoparticles with a diameter of 30 to 50 nm, which form of branched "antennas" on the phosphate core. According to the high-resolution TEM results (Fig. 5d), the nanoparticles layer consists of nickel oxyhydroxide (NiOOH has priority lattice fringes with interplanar distances of 0.688 and 0.344 nm, corresponding to the [111] and [222] lattice planes of NiOOH, # 96-901-2320).

Summarizing obtained results, we can propose the following conversion scheme for c-NNP material: (i) the formation of a  $\text{Ni}(\text{OH})_2$  layer on the phosphate surface is a consequence of the interaction of c-NNP and alkaline electrolyte to generation of  $\text{Na}_4\text{Ni}_3\text{P}_4\text{O}_{15}$ - $\text{Ni}(\text{OH})_2$  (core-shell) particles; (ii) under the conditions of the OOR process, partial oxidation of nickel hydroxide to NiOOH occurs, which is formed on the surface of  $\text{Ni}(\text{OH})_2$  as nanoparticles with a diameter range of 30–50 nm; (iii) NiOOH catalyst nanoparticles grow on the surface like bunches of grapes and form an additional layer on the surface that protects the core from further degradation. Thus, it is possible to assume the appearance of successive stable bound interfaces: c-NNP (core) -  $\text{Ni}(\text{OH})_2$  film (first shell) - NiOOH nanoparticles (second shell). According to XRD data, the core of such system is c-NNP (Fig. 4b), but XPS (Fig. 4d-h) and HR-TEM (Fig. 5d) results clearly indicate transformations in the surface layers. Combination of these results suggests that  $\text{Ni}(\text{OH})_2$  and NiOOH shells have both short-range order and long-range disordered structure. A similar situation was also previously observed after the OER process for other hybrid systems, as an example of  $\text{NiFe-OH-PO}_4$ .<sup>53</sup>

These facts indicate that a certain time is required for the formation of a stable electrolytic shell on the surface of c-NNP. Therefore, we previously provide stabilization of c-NNP-C/CC electrode for 10 hours at a current density of 10 mA·cm<sup>-2</sup> and then conduct an

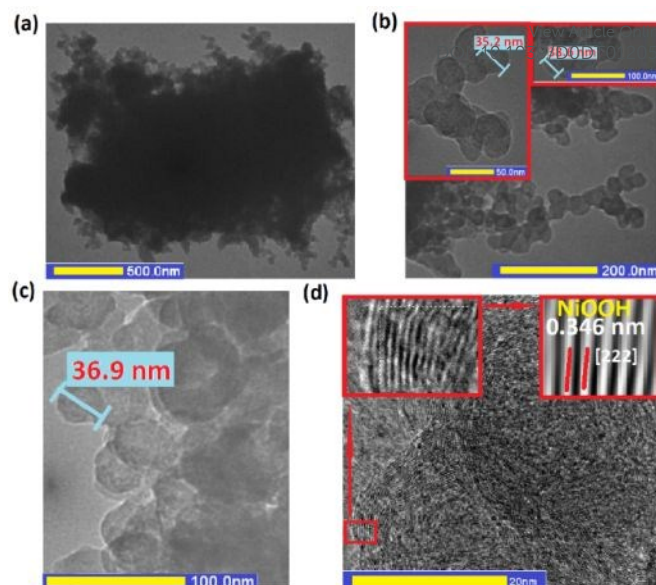


**Fig. 5** The results TEM for c-NNP-C/CC electrode after the long-term stability test for OER in 6 M KOH: (a) image c-NNP; (b) and (c) nanoparticles on surface of c-NNP at various magnifications; (d) high-resolution TEM of spherical nanoparticles.

additional maximum long-time CP test (more than 110 hours in 6 M KOH, Fig. 3g). It turned out that after stabilization, this electrode can provide an overpotential of 250 mV for OER at a current density of 10 mA·cm<sup>-2</sup>. During continuous electrolysis, this value slowly increases at 2.7, 7.4, and 13.8% in the 1st, 2nd, and 3rd days, respectively (Fig. 3g). After 80 hours of CP testing, the overpotential reaches a value of about 300 mV and the electrolyte becomes dark. Subsequently, intense evolution of oxygen bubbles continues to be observed, but particles begin to crumble from the electrode surface as result of carbon base destruction of the c-NNP-C/CC electrode. Over the next 30 hours, the carbon base continues to collapse, which is accompanied by an acceleration of overpotential growth (Fig. 3g). It should be also noted that overpotential values of OER for c-NNP-C/CC (and n-NNP-C/CC) electrodes are lower by about 30 mV in 6 M KOH than 6 M NaOH electrolyte (Fig. 3e). This effect is due to the fact that the conductivity of 6 M electrolyte KOH is almost twice higher in comparison as 6 M NaOH solution. Destruction energy of the hydration shell of K<sup>+</sup> ions is lower in comparison with shell Na<sup>+</sup> ions. Therefore, in our case, it should be expected a lower overpotential values of OER in the 6M KOH electrolyte. Moreover, overpotential values of oxygen evolution reaction for reference electrode  $\text{IrO}_2/\text{CC}$  were about 290 mV (6M KOH) and 330 mV (6M NaOH) at a current density of 10 mA·cm<sup>-2</sup> (Fig. 3c,d).

For the core-shell particles considered here overpotentials of OER are lower than many reported values for phosphates (Table S3, ESI †). Analyzing these results, we have evaluated following criteria: (i) stability and ways of transformation of the initial composition in highly alkaline solutions at OER condition; (ii) values of OER overpotential; (iii) electrocatalyst stability. Unfortunately, many reports do not discuss phosphate transformation after OER tests (Table S3, ESI †). Although, in recent years, a number of works describe transformation of phosphates in alkaline electrolytes after OER tests, but in most of them this question has not been discussed (Table S3, ESI †). A significant surface area of different nanoforms

promotes the rapid leaching of phosphate anions and the formation of *d*-metal hydroxides, which under OER conditions partially or completely transform to oxide-hydroxides. Phosphate anions can only dope oxide-hydroxides, as was observed for Ni<sub>2</sub>P<sub>4</sub>O<sub>12</sub>/CC<sup>52</sup> and Co-Fe-Pyro/GCE<sup>79</sup> electrodes. Partial preservation of the initial phosphate is possible only in the case of hybrid composites, in which the surface of the phosphate is already covered with a protective shell of hydroxides (as for the NiFe-OH-PO<sub>4</sub>/NF<sup>53</sup> electrode), or dense shell will be grown as a result of interaction with an alkaline solution. We assumed that in all cases, an oxide/hydroxide layer is formed on the surface of the phosphate with conditional composition MO<sub>x</sub>(OH)<sub>y</sub> (M – *d*-metal or metals) in an alkaline medium. Accordingly, for phosphate conversion products presented in Table S3, ESI †, following series of intervals can be created (values of OER overpotential at a current density of 10 mA·cm<sup>-2</sup>): FeNiO<sub>x</sub>(OH)<sub>y</sub> (200-300 mV)<sup>31,35,49,53,77</sup> < NiCoO<sub>x</sub>(OH)<sub>y</sub> (240-280 mV)<sup>41,48</sup> ≅ NiO<sub>x</sub>(OH)<sub>y</sub> (250-290 mV)<sup>47,52</sup> < CoFeO<sub>x</sub>(OH)<sub>y</sub> (260-290 mV)<sup>79</sup> < CoO<sub>x</sub>(OH)<sub>y</sub> (290-370 mV).<sup>45,46,54,58,80,81</sup> This general dependence has a good correlation with the results obtained for oxide/hydroxides. For example, the presence of iron in FeNiO<sub>x</sub>(OH)<sub>y</sub> increases the activity of Ni cations for OER.<sup>11-15</sup> A significant range of the obtained OER values for MO<sub>x</sub>(OH)<sub>y</sub> determine not only the composition, but also the morphology of the resulting nanostructure. This question should be considered separately, taking into account the type of initial phosphate morphology and the peculiarities of its transformation.

In general, stability of electrodes for OER is simultaneously affected by a significant number of factors: the morphology of electrocatalysts, material of electrode (current collector), presence of composite, which contributes to quickest possible electron transfer between catalyst and current collector. As can be seen from Table S3, ESI †, in comparison with other phosphate catalysts, Na<sub>4</sub>Ni<sub>3</sub>P<sub>4</sub>O<sub>15</sub>-Ni(OH)<sub>2</sub> particles display excellent catalytic activity toward OER, and are highly stable and durable, but CC base of fabricated electrodes are gradually destroyed in a strongly alkaline electrolyte under OER conditions. As noted above, fast formation of Na<sub>4</sub>Ni<sub>3</sub>P<sub>4</sub>O<sub>15</sub>-Ni(OH)<sub>2</sub> structure occurs in a highly alkaline medium or can be gradual when 0.1 M alkali solutions are used. This fact indicates additional capabilities. For example, an electrode can be first treated with an alkaline solution to form core-shell particles, and then used to water splitting in neutral or near-neutral electrolytes.<sup>29,30,60-62</sup> Such an idea may become as basis to number of future researches.

Thus, stable M-phosphate-MO<sub>x</sub>(OH)<sub>y</sub> (core-shell) particles can be basis to creating a new family of stable OER electrocatalysts. It should be expected that the use of multimetal phosphates (contain various combinations of *d*-metals) will allow a further decrease in overvoltage. At the same time, methods for creating core-shell particles require further improvement. These particles can be preliminarily prepared using various synthetic approaches or formed *in situ*. In the case of *in situ*, with purpose to preserve the phosphate core and formation of a reliable core-shell connection, transformation process of phosphate should be unhurried. Several ways can be suggested for this goal: (i) the use of ground crystalline phosphates (as was successfully demonstrated here); (ii) doping phosphate by ion, which increase its stability in an alkaline solution (for example, such as Ti, Zr or Hf); (iii) search among a wide variety of

complex phosphates compounds with increased stability in an alkaline medium. DOI: 10.1039/D0DT01205J

## Conclusions

In summary, it was shown that usage of various forms of mixed phosphate Na<sub>4</sub>Ni<sub>3</sub>P<sub>4</sub>O<sub>15</sub> (nanoparticles or crystals) allows generation of different types of nanosystems in alkaline solutions. The complete destruction of phosphate nanoparticles leads to appearance of 2D-nanosheets Ni(OH)<sub>2</sub>, while core-shell particles form from crystals. During electrolysis of water under OER conditions, a partial transformation of Ni(OH)<sub>2</sub> to NiOOH is realized for phosphate-carbon composites *in situ*. The resulting systems are excellent electrocatalysts for splitting water (requires an overpotential in rang 250-290 mV for OER at a current density of 10 mA·cm<sup>-2</sup> in 6 M KOH or NaOH electrolytes). Such a design is suitable to provide the low OER overvoltage value (250 mV at a current density of 10 mA·cm<sup>-2</sup>) with maximum long-term electrochemical stability (at least 70 hours) in 6 M KOH. Result analysis presented herein provides a new idea for the manufacture of highly efficient and highly durable phosphate based catalysts.

## Conflicts of interest

There are no conflicts to declare.

## Acknowledgements

This work was supported by the national long-term project [no. WQ20142200205] of “Thousand Talents Plan of Bureau of Foreign Experts Affairs” of People’s Republic of China and National Natural Science Foundation of China (NSFC Grant No.21571080), Natural Science Foundation of Jilin province (No. 20170101193JC).

## Notes and references

- X.X. Zou and Y. Zhang, *Chem. Soc. Rev.*, 2015, **44**, 5148-5180.
- H. Dau, C. Limberg, T. Reier, M Risch, S. Roggan and P. Strasser, *Chem. Cat. Chem.*, 2010, **2**, 724-761.
- N.-T. Suen, S.-F. Hung, Q. Quan, N. Zhang, Y.-J. Xu and H.M. Chen, *Chem. Soc. Rev.*, 2017, **46**, 337-365.
- Y. Lee, J. Suntivich, K.J. May, E.E. Perry and Y. Shao-Horn, *J. Phys. Chem. Lett.*, 2012, **3**, 399-404.
- N. Xu, G. Cao, Z. Chen, Q. Kang, H. Dai and P. Wang, *J. Mater. Chem. A.*, 2017, **5**, 12379-12384.
- M.-S. Balogun, Y. Huang, W. Qiu, H. Yang, H. Ji and Y. Tong, *Mater. Today*, 2017, **20**, 425-451.
- M. Shalom, D. Ressnig, X. Yang, G. Clavel, T.P. Fellingner and M. Antonietti, *J. Mater. Chem. A.*, 2015, **3**, 8171-8177.
- Z. Wu, Z. Zou, J. Huang and F. Gao, *J. Catal.*, 2018, **358**, 243-252.
- X. Yu, P. Xu, T. Hua, A. Han, X. Liu, H. Wu and P. Du, *Int. J. Hydrog. Energy*, 2014, **39**, 10467-10475.
- K. He, Z. Cao, R. Liu, Y. Miao, H. Ma and Y. Ding, *Nano Res.*, 2016, **9**, 1856-1865.
- M.W. Louie and A.T. Bell, *J. Am. Chem. Soc.*, 2013, **135**, 12329-12337.
- L. Trotochaud, S.L. Young, J.K. Ranney and S.W. Boettcher, *J. Am. Chem. Soc.*, 2014, **136**, 6744-6753.

- 13 D. Friebel, M. W. Louie, M. Bajdich, K. E. Sanwald, Y. Cai, A. M. Wise, M. J. Cheng, D. Sokaras, T. C. Weng, R. Alonso-Mori, R. C. Davis, J. R. Bargar, J. K. Nørskov, A. Nilsson and A. T. Bell, *J. Am. Chem. Soc.*, 2015, **137**, 1305-1313.
- 14 M. Steimecke, G. Seiffarth and M. Bron, *Anal. Chem.*, 2017, **89**, 10679-10686.
- 15 M. Görlin, J. Ferreira de Araújo, H. Schmies, D. Bernsmeier, S. Dresp, M. Gliuch, Z. Jusys, P. Chernev, R. Kraehnert, H. Dau and P. Strasser, *J. Am. Chem. Soc.*, 2017, **139**, 2070-2082.
- 16 T. Wang, X. Zhang, X. Zhu, Q. Liu, S. Lu, A.M. Asiri, Y. Luo and X. Sun, *Nanoscale*, 2020, **12**, 5359-5362.
- 17 H.-W. Man, C.-S. Tsang, M.M.-J. Li, J. Mo, B. Huang, L.Y.S. Lee, Y.-C. Leung, K.-Y. Wong and S.C.E. Tsang, *Chem. Commun.*, 2018, **54**, 8630-8633.
- 18 G.-F. Chen, T. Yi Ma, Z.-Q. Liu, N. Li, Y.-Z. Su, K. Davey and S.-Z. Qiao, *Adv. Funct. Mater.*, 2016, **26**, 3314-3323.
- 19 J. Li, G. Wei, Y. Zhu, Y. Xi, X. Pan, Y. Ji, I.V. Zatovsky and W. Han, *J. Mater. Chem. A.*, 2017, **5**, 14828-14837.
- 20 Y. Zhu, C. Lv, Z. Yin, J. Ren, X. Yang, C.-L. Dong, H. Liu, R. Cai, Y.-C. Huang, W. Theis, S. Shen and D. Yang, *Angew. Chem. Int. Ed.*, 2020, **59**, 868-873.
- 21 Y. Zhu, J. Li, J. Cao, C. Lv, G. Huang, G. Zhang, Y. Xu, S. Zhang, P. Meng, T. Zhan and D. Yang, *APL Mater.*, 2020, **8**, 041108.
- 22 K. Wan, J. Luo, C. Zhou, T. Zhang, J. Arbiol, X. Lu, B.-W. Mao, X. Zhang and J. Fransaer, *Adv. Funct. Mater.*, 2019, **29**, 1900315.
- 23 S. Debata, S. Patra, S. Banerjee, R. Madhuri and P.K. Sharma, *Appl. Surf. Sci.*, 2018, **449**, 203-212.
- 24 J. Bao, X. Zhang, B. Fan, J. Zhang, M. Zhou, W. Yang, X. Hu, H. Wang, B. Pan and Y. Xie, *Angew. Chem. Int. Ed.*, 2015, **54**, 7399-7404.
- 25 Y.J. Sa, K. Kwon, J.Y. Cheon, F. Kleitz and S.H. Joo, *J. Mater. Chem. A.*, 2013, **1**, 9992-10001.
- 26 W.T. Hong, M. Risch, K.A. Stoerzinger, A. Grimaud, J. Suntivich and Y. Shao-Horn, *Energy Environ. Sci.*, 2015, **8**, 1404-1427.
- 27 R. K. Hona and F.D. Ramezanipour, *Angew. Chem. Int. Ed.*, 2019, **58**, 2060-2063.
- 28 J. Liu, Y. Ji, J. Nai, X. Niu, Y. Luo, L. Guo and S. Yang, *Energy Environ. Sci.*, 2018, **11**, 1736-1741.
- 29 C. You, Y. Ji, Z. Liu, X. Xiong and X. Sun, *ACS Sustainable Chem. Eng.*, 2018, **6**, 1527-1531.
- 30 R. Ge, M. Ma, X. Ren, F. Qu, Z. Liu, G. Du, A.M. Asiri, L. Chen, B. Zheng and X. Sun, *Chem. Commun.*, 2017, **53**, 7812-7815.
- 31 Y. Li and C. Zhao, *Chem. Mater.*, 2016, **28**, 5659-5666.
- 32 J. Xing, H. Li, M.M.-C. Cheng, S.M. Geyer and K. Y. Simon Ng, *J. Mater. Chem. A.*, 2016, **4**, 13866-13873.
- 33 Y. Yang, H. Fei, G. Ruan and J.M. Tour, *Adv. Mater.*, 2015, **27**, 3175-3180.
- 34 F. Massel, S. Ahmadi, M. Hahlin, Y.-S. Liu, J.-H. Guo, T. Edvinsson, H. Rensmo and L.-C. Duda, *J. Electron Spectros. Relat. Phenomena*, 2018, **224**, 3-7.
- 35 Y. Liu, H. Wang, D. Lin, C. Liu, P.-C. Hsu, W. Liu, W. Chen and Y. Cui, *Energy Environ. Sci.*, 2015, **8**, 1719-1724.
- 36 Y. Zhan, M. Lu, S. Yang, C. Xu, Z. Liu and J.Y. Lee, *Chem. Cat. Chem.*, 2016, **8**, 372-379.
- 37 J. Wang, Y. Xie, Y. Yao, X. Huang, M. Willinger and L. Shao, *J. Mater. Chem. A.*, 2017, **5**, 14758-14762.
- 38 H. Kim, J. Park, I. Park, K. Jin, S.E. Jerng, S.H. Kim, K.T. Nam and K. Kang, *Nat. Commun.*, 2015, **6**, 8253-8264.
- 39 M. Pramanik, C. Li, M. Imura, V. Malgras, Y.-M. Kang and Y. Yamauchi, *Small*, 2016, **12**, 1709-1705.
- 40 D. Yin, Z. Jin, M. Liu, T. Gao, H. Yuan and D. Xiao, *Electrochim. Acta*, 2018, **260**, 420-429.
- 41 J. Li, W. Xu, D. Zhou, J. Luo, D. Zhang, P. Xu, L. Wei and D. Yuan, *J. Mater. Sci.*, 2018, **53**, 2077-2086.
- 42 Y. Zhan, S. Yang, M. Lu, Z. Liu and J.Y. Lee, *Electrochim. Acta*, 2017, **227**, 310-316.
- 43 R. Guo, X. Lai, J. Huang, X. Du, Y. Yan, Y. Sun, G. Zou and J. Xiong, *ChemElectroChem*, 2018, **5**, 3822-3834.
- 44 L. Yang, Z. Guo, J. Huang, Y. Xi, R. Gao, G. Su, W. Wang, L. Cao and B. Dong, *Adv. Mater.*, 2017, **29**, 1704574.
- 45 C. Yuan, Y. Jiang, Z. Wang, X. Xie, Z. Yang, A. B. Yousaf and A. Xu, *J. Mater. Chem. A.*, 2016, **4**, 8155-8160.
- 46 P. K. Katkar, S. J. Marje, S. B. Kale, A. C. Lokhande, C. D. Lokhande and U. M. Patil, *CrystEngComm.*, 2019, **21**, 884-893.
- 47 S.J. Marje, P.K. Katkar, S.B. Kale, A.C. Lokhande, C.D. Lokhande and U.M. Patil, *Journal of Alloys and Compounds*, 2019, **779**, 49-58.
- 48 C. Zhao, P. Li, D. Shao, R. Zhang, S. Wang, Z. Zhu and C. Zhao, *Int. J. Hydrog. Energy.*, 2019, **44**, 844-852.
- 49 S. Ma, Q. Zhu, L. Chen, W. Wang and D. Chen, *J. Mater. Chem. A.*, 2016, **4**, 8149-8154.
- 50 C. Murugesan, S. Lochab, B. Senthilkumar and P. Barpanda, *ChemCatChem.*, 2018, **10**, 1122-1127.
- 51 R. Gond, K. Sada, B. Senthilkumar and P. Barpanda, *ChemElectroChem.*, 2018, **5**, 153-158.
- 52 J. W. Huang, Y. H. Sun, Y. D. Zhang, G. F. Zou, C. Y. Yan, S. Cong, T. Y. Lei, X. Dai, J. Guo, R. F. Lu, Y. R. Li and J. Xiong, *Adv. Mater.*, 2018, **30**, 1705045.
- 53 Z. Lei, J. Bai, Y. Li, Z. Wang and C. Zhao, *ACS Appl. Mater. Interfaces*, 2017, **9**, 35837-35846.
- 54 R. Gond, D. K. Singh, M. Eswaramoorthy and P. Barpanda, *Angew. Chem. Int. Ed.*, 2019, **58**, 8330-8335.
- 55 M. S. Islam and C. A. J. Fisher, *Chem. Soc. Rev.*, 2014, **43**, 185-204.
- 56 J.-Y. Hwang, S.-T. Myung and Y.-K. Sun, *Chem. Soc. Rev.*, 2017, **46**, 3529-3614.
- 57 R. Gond, R. P. Rao, V. Pralong, O. I. Lebedev, S. Adams, and P. Barpanda, *Inorg. Chem.*, 2018, **57**, 6324-6332.
- 58 I.V. Odynets, N.Yu. Strutynska, J. Li, W. Han, I.V. Zatovsky and N.I. Klyui, *Dalton Trans.*, 2018, **47**, 15703-15713.
- 59 J. Chang, Q. Lv, G. Li, J. Ge, C. Liu and W. Xing, *Appl. Catal. B*, 2017, **204**, 486-496.
- 60 L. Xie, R. Zhang, L. Cui, D. Liu, S. Hao, Y. Ma, G. Du, A.M. Asiri and X. Sun, *Angew. Chem. Int. Ed.*, 2017, **56**, 1064-1068.
- 61 M. Ma, F. Qu, X. Ji, D. Liu, S. Hao, G. Du, A.M. Asiri, Y. Yao, L. Chen and X. Sun, *Small*, 2017, 1700394.
- 62 G. Zhu, L. Yang, R. Zhang, F. Qu, Z. Liu, G. Du, A.M. Asiri, Y. Yao and X. Sun, *Nanoscale*, 2017, **9**, 12343-12347.
- 63 R. Zhang, Z. Wang, S. Hao, R. Ge, X. Ren, F. Qu, G. Du, A.M. Asiri, B. Zheng and X. Sun, *ACS Sustainable Chem. Eng.*, 2017, **5**, 8518-8522.
- 64 D. Wu, Y. Wei, X. Ren, X. Ji, Y. Liu, X. Guo, Z. Liu, A.M. Asiri, Q. Wei and X. Sun, *Adv. Mater.*, 2018, **30**, 1705366.
- 65 W. Lu, T. Liu, L. Xie, C. Tang, D. Liu, S. Hao, F. Qu, G. Du, Y. Ma, A.M. Asiri and X. Sun, *Small*, 2017, **13**, 1700805.
- 66 S. M. Wood, C. Eames, E. Kendrick, and M. S. Islam, *J. Phys. Chem. C.*, 2015, **119**, 15935-15941.
- 67 B. Senthilkumar, G. Ananya, P. Ashok, and S. Ramaprabhu, *Electrochimica Acta*, 2015, **169**, 447-455.
- 68 F. Sanz, C. Parada, J. M. Rojo and C. Ruiz-Valero, *Chem. Mater.*, 2001, **13**, 1334-1340.
- 69 P.G. Nagorny, A.A. Kapshuk, A.N. Sobolev and N.V. Golego, *Crystallogr. Rep.*, 1996, **41**, 793-796.
- 70 N.Yu. Strutynska, I.V. Zatovsky, M.M. Yatskin, N.S. Slobodyanik and I.V. Ogorodnyk, *Inorganic Materials*, 2012, **48**, 402-406.
- 71 I.V. Zatovsky, N.Yu. Strutynska, Yu.A. Hizhnyi, V.N. Baumer, I.V. Ogorodnyk, N.S. Slobodyanik, I.V. Odynets and N.I. Klyui, *Dalton Trans.*, 2018, **47**, 2274-2284.
- 72 C. Wagner, L. Davis, M. Zeller, J. Taylor, R. Raymond and L. Gale, *Surface and Interface Analysis*, 1981, **3**, 211-225.
- 73 R. Ding, L. Qi and H. Wang, *Electrochimica Acta*, 2013, **114**, 726-735.

## Journal Name

## ARTICLE

- 74 D.H. Li, D.J. Yang, X.Y. Zhu, D.W. Jing, Y.Z. Xia, Q. Ji, R.S. Cai, H.L. Li and Y.K. Che, *J. Mater. Chem. A*, 2014, **2**, 18761–18766.
- 75 S. Niu, W.-J. Jiang, T. Tang, Y. Zhang, J-H. Li and J-S Hu, *Adv. Sci.*, 2017, 1700084.
- 76 D.V. Esposito, *Joule*, 2017, **1**, 651–658.
- 77 X. Wu, Y. Zhao, T. Xing, P. Zhang, F. Li, H. Lee, F. Li and L. Sun, *ChemSusChem*, 2018, **11**, 1761–1767.
- 78 L. Qian, Z. Lu, T. Xu, X. Wu, Y. Tian, Y. Li, Z. Huo, X. Sun and X. Duan, *Adv. Energy Mater.*, 2015, **5**, 1500245.
- 79 M. Liu, Z. Qu, D. Yin, X. Chen, Y. Zhang, Y. Guo and D. Xiao, *ChemElectroChem*, 2018, **5**, 36–43.
- 80 L. Ai, Z. Niu and J. Jiang, *Electrochim. Acta*, 2017, **242**, 355–363.
- 81 J. Wang and H. C. Zeng, *ACS Appl. Mater. Interfaces*, 2018, **10**, 6288–6298.

View Article Online  
DOI: 10.1039/D0DT01205J

Dalton Transactions Accepted Manuscript